Journal of Geophysical Research: Solid Earth

RESEARCH ARTICLE
10.1029/2017JB015260

Key Points:
- The electrical resistivity of pure iron, $Fe_{99}C_1$, and iron carbides (Fe_3C and Fe_7C_3) was measured at pressures up to 80 GPa
- Carbon has a stronger alloying effect in reducing the electrical and thermal conductivities in the Earth's core than that of Si, S, and Ni
- Earth's core in an Fe-C composition will have a low heat flow at the core-mantle boundary and a conductivity gap at the inner-core boundary

Supporting Information:
- Supporting Information S1

Correspondence to:
J.-F. Lin,
afu@jsg.utexas.edu

Citation:
Zhang, C., Lin, J.-F., Liu, Y., Feng, S., Jin, C., Hou, M., & Yoshino, T. (2018). Electrical resistivity of Fe-C alloy at high pressure: Effects of carbon as a light element on the thermal conductivity of the Earth's core. *Journal of Geophysical Research: Solid Earth*, *123*. https://doi.org/10.1029/2017JB015260

Received 24 NOV 2017
Accepted 29 APR 2018
Accepted article online 5 MAY 2018

Electrical Resistivity of Fe-C Alloy at High Pressure: Effects of Carbon as a Light Element on the Thermal Conductivity of the Earth's Core

Chengwei Zhang[1], Jung-Fu Lin[2], Ying Liu[3], Shaomin Feng[3], Changqing Jin[3], Mingqiang Hou[1], and Takashi Yoshino[4]

[1]Center for High Pressure Science and Technology Advanced Research (HPSTAR), Shanghai, China, [2]Department of Geological Sciences, Jackson School of Geosciences, The University of Texas at Austin, Austin, TX, USA, [3]Key Laboratory of Extreme Conditions Physics, Institute of Physics, Chinese Academy of Science, Beijing, China, [4]Institute for Planetary Materials, Okayama University, Misasa, Tottori, Japan

Abstract We measured the electrical resistivity of iron, $Fe_{99}C_1$, Fe_3C, and Fe_7C_3 up to ~80 GPa using the van der Pauw method in a diamond anvil cell. The electrical resistivity of disordered $Fe_{99}C_1$ at high pressure shows a strong impurity resistivity of carbon. The ferromagnetic-paramagnetic transition in Fe_3C and Fe_7C_3 is associated with the flattening of the resistivity pressure gradient at ~6 GPa. Fe_7C_3 exhibits the highest electrical resistivity among all iron-light element alloys, and Fe_3C and Fe_7C_3 disobey the Matthiessen's rule by showing a lower electrical resistivity than a disordered iron-carbon alloy because of chemical ordering. A comparison of the impurity resistivity between silicon, sulfur, nickel, and carbon shows that carbon has an exceedingly stronger alloying effect than other elements. If the chemical ordering observed in Fe-Si system is held true for the Fe-C system, the chemical ordering in Fe_7C_3 possibly increases the thermal conductivity of the inner core and enlarges the thermal and electrical conductivity gap at the inner-core boundary. Models of the thermal conductivity of liquid $Fe_{70}C_{30}$ with 8.4 wt % carbon show a low thermal conductivity of 38 Wm^{-1} K^{-1} at the pressure-temperature conditions of the topmost outer core. The corresponding heat flow of 6 TW at the core-mantle boundary is notably lower than previous electrical resistivity results on Fe and Fe alloys. The alloying effect of carbon on the electrical and thermal conductivity of iron can thus play a significant role in understanding the heat flux at the core-mantle boundary and the thermal evolution of the core.

1. Introduction

Earth's magnetic fields are generated in the outer core through dynamic motions of the molten iron alloy. Secular cooling at the uppermost outer core solidifies the inner core, during which latent heat and incompatible light elements are released from the inner core into the outer core. The thermal turbulence of the outer core and compositional buoyancy due to the release of light elements are believed to provide the major energy source required to power the geodynamo (Lay et al., 2008; Stevenson, 2008). Conductive heat flow depends on temperature gradient and thermal conductivity of the iron alloy at the uppermost outer core and constrains the energy of fluid alloy convection, which drove the geodynamo to generate the geomagnetic field at least 3 billion years ago before the inner core was formed (Buffett, 2003). The thermal conductivity in the outer core is also closely correlated with the growth rate and age of the inner core, the presence of radiogenic materials, and the formation of a stratified layer below the core-mantle boundary (CMB; Buffett, 2016; Lay et al., 2008; Lister & Buffett, 1998). Thus, knowing the thermal transport property of the candidate iron alloys at conditions relevant to the Earth's core is vital to understand the geomagnetic and geodynamic conundrums of Earth's core (Gomi et al., 2013; Nimmo, 2007; Olson, 2013). A recent direct measurement of the thermal conductivity at high pressure and temperature (Konôpková et al., 2016) approaching Earth's core impugns the high value of the thermal conductivity determined by electrical measurement (Gomi et al., 2013; Gomi & Hirose, 2015; Ohta et al., 2016; Seagle et al., 2013). These studies create new disputes on the available energy source for Earth's geodynamo, the total heat flow across the CMB, and thermal evolution and history of the core (Dobson, 2016; Labrosse, 2015; Olson, 2013).

Based on geophysical and geochemical arguments, the Earth's core also contains significant amounts of light elements—approximately ~10 wt % for the outer core (Li & Fei, 2003) and ~3–8 wt % for the inner core (Alfè

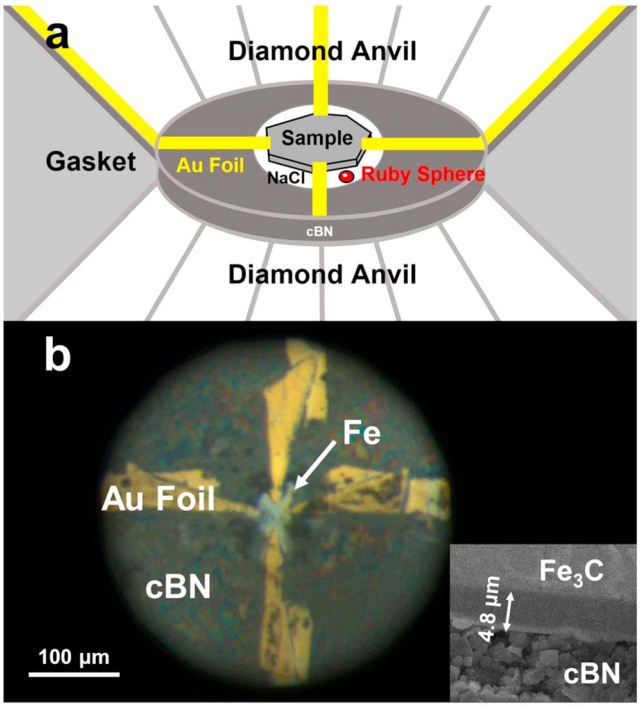

Figure 1. High-pressure electrical resistivity measurements of iron and iron-carbon alloys in a diamond anvil cell (DAC). (a) Schematics of the sample chamber configuration for a four-probe measurement in a DAC. (b) Photograph of the sample chamber with iron at 0.5 GPa taken with a reflected light source. The figure insert in (b) is a focused ion beam micrograph of a representative cross section of the quenched Fe_3C sample from 50.7 GPa. The quenched sample measured 4.8 μm thick at ambient pressure, which was used with its equation of state to evaluate the electrical resistivity of the sample at high pressures. A cubic boron nitride (cBN) insert was used as the electrical insulation, while dried NaCl was used as the pressure medium. Four pieces of Au foil were placed on cBN and used as electrodes in contact with the sample for the electrical resistivity experiments based on the van der Pauw method.

et al., 2007; Badro et al., 2007; Mao et al., 2012). Based on the cosmochemical, geochemical, and geophysical evidence, several elements, including H, C, S, O, and Si, have been suggested to alloy with iron in the core (Li & Fei, 2003; Poirier, 1994). Previous studies employing electrical resistivity measurements have investigated the pressure-temperature effect (Ohta et al., 2016) and impurity resistivity of nickel (Gomi & Hirose, 2015), silicon (Gomi et al., 2013, 2016; Seagle et al., 2013), and sulfur (Suehiro et al., 2017). These experiments reveal the significance of the thermal and light element effects that are capable of significantly altering the high-pressure thermal conductivity of iron alloys. However, the impurity effect of the remaining candidate light elements in the core has not yet been investigated, though their great impact on the physical properties of the core has been broadly discussed (Hirose et al., 2013).

Carbon is considered a probable light element to be present in Earth's core because of its abundance in the solar system and in CI carbonaceous chondrites. Additionally, at the thermodynamic conditions relevant to the Earth's core, several iron-carbon alloys are stable (Liu et al., 2016b; Poirier, 1994; Wood, 1993; Wood et al., 2013). A number of iron-carbon alloys including Fe-rich Fe-C alloy, Fe_3C, and Fe_7C_3 are suggested by high-pressure experiments to be candidate carbon-bearing phases in Earth's core. Since the solubility of carbon in solid Fe is considered to be relatively low in Earth's core conditions, intermediate Fe-C compounds (Fe_3C and Fe_7C_3) have been more extensively investigated (Chen et al., 2012, 2014; Fei & Brosh, 2014; Gao et al., 2008, 2011; Liu et al., 2016a; Lord et al., 2009). Cementite (Fe_3C), a stable iron carbide in the Fe-C system, is an intermediate compound with an orthorhombic structure (*Pnma*), which undergoes a magnetic phase transition from a ferromagnetic (FM) to a paramagnetic (PM) state at its Curie temperature of 483 K at 1 atm (Wood et al., 2004). This magnetic phase transition can also be pressure-induced at 4.3–10 GPa and room temperature, as determined by different X-ray spectroscopic methods (Duman et al., 2005; Gao et al., 2008; Litasov et al., 2013; Prescher et al., 2012). Theoretical approaches (Mookherjee, 2011; Vočadlo et al., 2002) also predicted that, at 60 GPa, Fe_3C would transform from a PM to a nonmagnetic (NM) phase, and a high-spin to low-spin transition without major structural transformation was experimentally observed by synchrotron Mössbauer spectroscopy (SMS; Prescher et al., 2012) at 22 GPa and X-ray emission spectroscopy (Lin et al., 2004) at 25 GPa. Cementite was first proposed to be a potential carbon-bearing compound in the Earth's core due to it high P-T stability (Wood, 1993). Sound velocity studies on Fe_3C provide further evidence of this conclusion (Gao et al., 2008, 2011; Mookherjee, 2011). Another carbon-bearing phase, Fe_7C_3, is increasingly suggested to be a more stable inner-core phase by recent theoretical and experimental studies (Liu et al., 2016b; Lord et al., 2009; Mookherjee, 2011; Nakajima et al., 2011). Fe_7C_3 can take on two different crystal structures at such conditions: a hexagonal structure (*h*-Fe7C3) with the space group $P6_3mc$ and an orthorhombic structure (*o*-Fe7C3) with a possible space group of *Pnma*, *Pmcn*, or *Pbca* (Liu et al., 2016a). Like cementite, Fe_7C_3 goes through a magnetic transition from FM to PM at its Curie temperature of 523 K (Tsuzuki et al., 1984). Based on changes in its compression curve and axial ratio, the FM to PM transition at 300 K was determined to take place at 18 GPa (Nakajima et al., 2011)—similar to the value of 16 GPa determined via a combined X-ray powder diffraction (XRD) and SMS study (Prescher et al., 2015). A smaller value of 5.5–7.5 GPa for the FM-PM transition and a PM-NM transition at 53 GPa were determined using XRD and SMS (Chen et al., 2012, 2014). An elastic softening associated with FM-PM transition was also observed by XRD experiments at 7–20 GPa (Liu et al., 2016a). A theoretical study (Mookherjee, 2011) determined that the PM-NM transition occurred at 67 GPa, corroborating an experimental study, which observed the transition at 70 GPa (Prescher et al., 2015). In sound velocity measurement studies, Fe_7C_3 displays a high Poisson's ratio and a shear softening

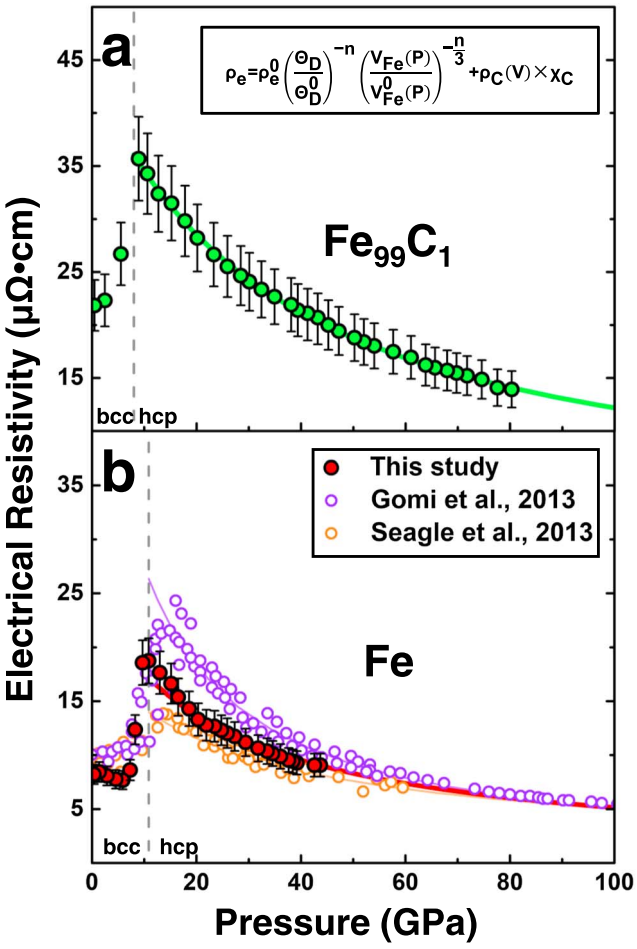

Figure 2. Electrical resistivity of (a) $Fe_{99}C_1$ and (b) Fe at high pressures and room temperature. As shown by the vertical gray dashed lines, $Fe_{99}C_1$ undergoes a bcc-hcp transition at ~8.0 GPa, while pure Fe undergoes the transition at ~10.9 GPa. The solid green and red lines are the modeled fits to the experimental data in this study (solid circles) for hcp-$Fe_{99}C_1$ and hcp-Fe, respectively. Previous experimental diamond anvil cell results for Fe (purple and orange circles) with modeled fits are also shown here for comparison (Gomi et al., 2013; Seagle et al., 2013). The equation used for the modeling is shown in the box insert.

at Earth's core conditions, conforming to seismic observations that support Fe_7C_3 as a candidate phase in the inner core (Chen et al., 2014; Prescher et al., 2015).

To provide new insight on the thermal conduction of iron alloys in the Earth's core, we investigated the light element effect of carbon on the resistivity of iron at high pressures. We conducted van der Pauw four-probe measurements on iron-carbon alloy ($Fe_{99}C_1$) and carbides (Fe_3C and Fe_7C_3), as well as pure iron using a high-pressure diamond anvil cell (DAC) up to ~80 GPa. We then established several models for the electrical resistivity of the pure iron, iron-carbon alloys, and iron carbides and the thermal conductivity of different iron alloys along with a representative core geotherm. Together with previous electrical resistivity and thermal conductivity results on Fe, Fe-Ni, Fe-Si, and Fe-Si-S alloy, we made a thorough comparison of the alloying effects of these different elements on the transport properties and analyzed the magnitude and variation of the thermal conduction along the pressure and temperature paths in the Earth's core. With this knowledge of the light element effects on thermal conductivity, the Fe-C system gives a new insight into the controversy about the amount of heat conduction produced from the core. We demonstrate that a thermal conductivity model with different light element compositions provides significant constraints for determining the age and thermal evolution of Earth's core.

2. Experiments

The Fe_3C starting sample was synthesized from a mixture of iron and graphite powder (>99.99% purity) in an atomic ratio of 3:1 at the Institute for Planetary Materials, Okayama University at Misasa. The mixture was packed into an MgO capsule and then loaded into a piston cylinder apparatus and left to equilibrate at 1,373 K and ambient pressure for 18 hr. The same sample was used in Liu et al. (2016b) for a melting and phase transition study. Fe_7C_3 was synthesized by a carbon diffusion method to avoid the appearance of an additional phase caused by a weighing error. The Fe rod (99.5% purity) was placed in a graphite capsule (Ibiden Co. T-5) insulated by MgO from the $LaCrO_3$ heater. The sample was annealed at 14 GPa and 1,773 K for 2 hr in a Kawai-type multianvil press at the Institute for Planetary Materials, Okayama University at Misasa. Fe_7C_3 was formed by carbon diffusion into iron. After annealing, the sample was cooled to 1,473 K and kept for 1 hr. The sample was removed from the surrounding diamond. All iron carbide samples were analyzed using XRD and electronic microprobe analyses to confirm their composition and structure. $Fe_{99}C_1$ (contains 0.2 wt % carbon) was purchased commercially from the National Institute of Standards and Technology. Fe_3C and Fe_7C_3 were both confirmed to be polycrystalline single phases in the orthorhombic structure (space group: *Pnma*), while $Fe_{99}C_1$ was confirmed to have a body-centered cubic (bcc) structure at ambient conditions. Based on XRD analysis, the lattice parameters of Fe_3C are $a = 5.092$ Å, $b = 6.751$ Å, and $c = 4.514$ Å and $a = 4.536$ Å, $b = 6.892$ Å, and $c = 11.915$ Å for Fe_7C_3. These results are consistent with previous reports (Li et al., 2002; Nakajima et al., 2011). A tungsten carbide drill bit was used to break off some of the sample pellets into small pieces of a few tens of μm in diameter. A few pieces of the iron carbide sample were then selected and compressed between two flat 200-μm culets in a DAC to make flat disks of ~5–10 μm thick with homogenous thickness and smooth surfaces. These are required for reliable electrical conductivity measurements using the van der Pauw method (Seagle et al., 2013; van der Pauw, 1958).

Four-probe electrical resistivity experiments were performed in high-pressure DACs with either a pair of 400 or 200-μm flat culets at the Key Laboratory of Extreme Conditions Physics, Institute of Physics, Chinese

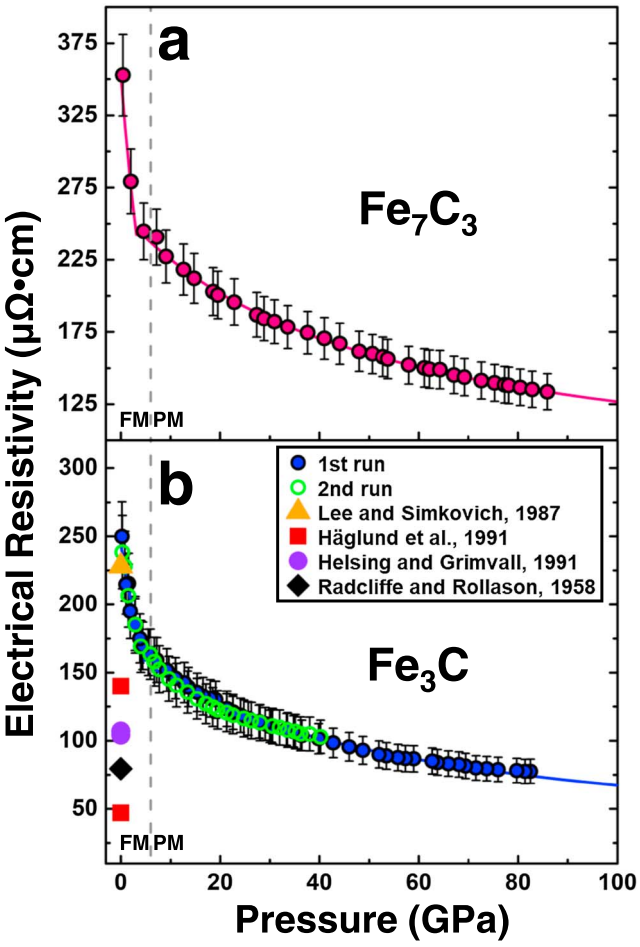

Figure 3. Electrical resistivity of (a) Fe_7C_3 and (b) Fe_3C at high pressures and room temperature. As shown by the vertical gray dashed lines, Fe_7C_3 and Fe_3C undergo the ferromagnetic to paramagnetic (PM) transition at ~6 GPa, respectively, such that the resistivity of each state has been modeled independently (shown as solid magenta and blue lines). The modeled results of the PM state are used for further high-pressure modeling of Earth's core P-T conditions. Circles: Fe_7C_3 (solid magenta circles), first run (solid blue circles), and second run (green open circles) for Fe_3C in this study; orange triangle: Fe_3C at ambient conditions (Lee & Simkovich, 1987); red squares, purple circles, and black diamond: previous calculated electrical resistivity of Fe_3C at ambient conditions (Häglund et al., 1991; Helsing & Grimvall, 1991; Radcliffe & Rollason, 1958).

Academy of Sciences. A stainless-steel gasket was pre-indented to approximately 25 GPa with a thickness of 50 μm with 400-μm culets or 30 μm with 200-μm culets. Nearly four-fifth of the pre-indented area was drilled out with a YAG laser. Subsequently, a cubic boron nitride (cBN) gasket insert was packed into the drilled hole and onto the area of the gasket surrounding the indentation and compressed to approximately 25 GPa. The second hole with a diameter of approximately 30 μm was then drilled on the compacted cBN insert, which served as the sample chamber. Dried NaCl (sodium chloride) was put into the chamber as a layer of pressure transmitting medium. Then, a piece of the flattened sample was placed onto NaCl layer, and a ruby sphere was placed near the sample as the pressure calibrant (Figure 1). Four gold foils in a wedged-shape were laid onto the cBN insert and slightly compressed between the diamond anvils to make good contact with the sample. The use of the cBN gasket insert also provided good electrical insulation to avoid possible contact of the stainless-steel gasket with the gold electrodes and the sample (Figure 1). The pressure of the sample chamber was monitored by the ruby fluorescence (Mao et al., 1986).

A four-probe system consisting a source meter (Keithley 2400) and a nanovoltage meter (Keithley 2182A) with an output current of ~1–5 mA was used for the electrical conductivity measurements at high pressure and room temperature. The four-probe method was used to minimize the resistivity contribution from the electrical leads and contact resistance (Seagle et al., 2013; van der Pauw, 1958) and to reliably determine the resistivity of an arbitrary-shaped sample with an even thickness (van der Pauw, 1958). A detailed description of the method and calculation of the electrical resistivity from the four-probe measurements can be found in the previous literature (Seagle et al., 2013; van der Pauw, 1958). The electrical resistance of the sample was measured upon compression and decompression up to ~40 GPa for pure Fe and ~80 GPa for $Fe_{99}C_1$, Fe_3C, and Fe_7C_3. In previous studies the geometry of the sample was reported to deform under compression (Gomi et al., 2013; Seagle et al., 2013). We present and compare our data (Figure S1 in the supporting information) during both compression and decompression in the supporting information but have only used the data on decompression here (Figures 2 and 3) for further evaluation and analysis of the samples' resistivity at high pressures to be consistent with the approach used in previous studies (Seagle et al., 2013). To determine the thickness of the samples, the decompressed and recovered samples in gasket chambers were cut and analyzed using the focused ion beam (FIB Model: FEI Versa 3D) at the Center for High Pressure Science and Advanced Technology (HPSTAR), Shanghai (Figure 1b). These measured sample thicknesses were then used with the equation of state of the samples, respectively, to evaluate each sample's thickness and electrical conductivity at high pressures (Dewaele et al., 2006; Li et al., 2002; Nakajima et al., 2011).

3. Results on the Electrical Resistivity of Iron Carbon Alloys at High Pressure

The variation in electrical resistivity with the increasing pressure of $Fe_{99}C_1$ is similar to that of pure iron (Figure 2). However, the electrical resistivity of $Fe_{99}C_1$ is ~10–15 μΩ cm larger than that of Fe at ambient conditions and in the hcp phase at approximately 12 GPa (Figure 2b). Such a large electrical resistivity of $Fe_{99}C_1$ at high pressures might be due to the previously reported frustration of the local magnetic ordering in the Fe-C alloy (Medvedeva et al., 2010). The increase in resistivity during decompression at ~11 GPa, followed by a sudden drop at 8 GPa, is indicative of the back transition of the hexagonal close-packed (hcp) to bcc phase in the

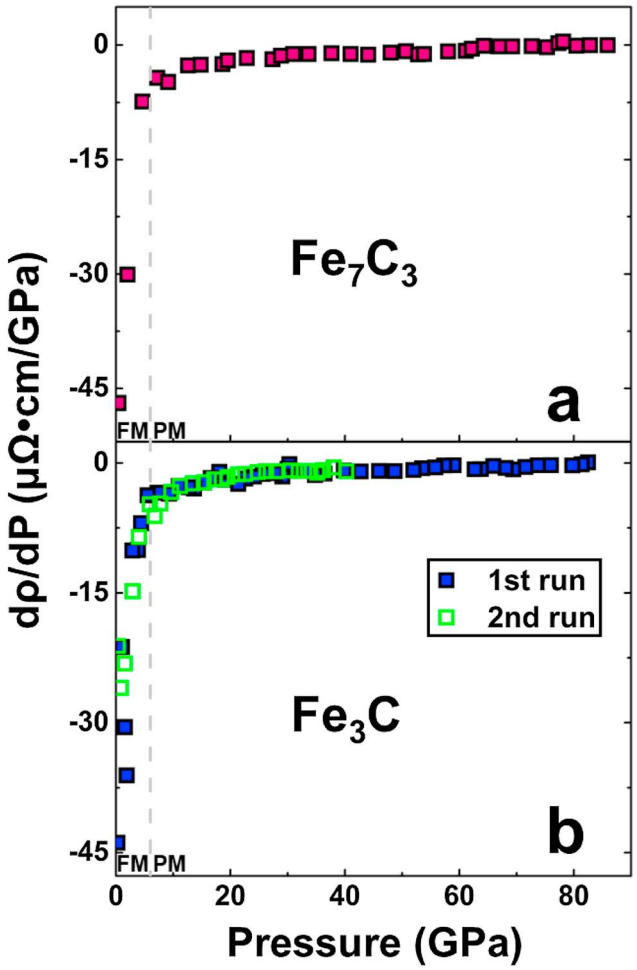

Figure 4. First-order pressure derivative of the electrical resistivity of (a) Fe_7C_3 and (b) Fe_3C (dρ/dP) at high pressures. The drastic change in the derivative for Fe_7C_3 and Fe_3C at approximately 6 GPa is attributed to the ferromagnetic to paramagnetic (PM) transition reported previously (Chen et al., 2012, 2014; Duman et al., 2005; Gao et al., 2008; Litasov et al., 2013; Prescher et al., 2012). The flattening of the pressure derivative in the PM state indicates that the high-pressure effect on the electrical resistivity significantly decreases with increasing pressure.

alloy. This has also been reported for iron-rich iron-silicon and iron-nickel alloys (Gomi et al., 2016; Gomi & Hirose, 2015). The resistivity of $Fe_{99}C_1$ is considered higher than pure iron over the entire pressure range—a clear sign of the alloy effect (Figure 2). Our hcp-Fe electrical resistivity values are in-between two recent electrical resistivity measurements of iron using a DAC (Gomi et al., 2013; Seagle et al., 2013; Figure 2b). The discrepancy between our result and previous works is considered normal and within experimental uncertainty. A jump in the resistivity of iron is observed at ~11 GPa on decompression, which can be attributed to the hcp to bcc phase transition. By comparing the electrical resistivity of iron during compression and decompression (Figure S1a), the known sluggish phase transition of iron between bcc and hcp is manifested by the drastic change of electrical resistivity. Under compression, the forward transition from bcc to hcp starts at ~14 GPa and finishes at ~18 GPa. Upon decompression, the reverse transition from hcp to bcc starts at ~11 GPa and finishes at ~6 GPa. The hysteresis caused by incomplete relaxation during compression and decompression agrees with previous reports (Giles et al., 1971). Similar hysteresis in the electrical conductivity across the bcc-hcp transition has also been observed in the $Fe_{99}C_1$ alloy during compression and decompression (Figure S1b). However, a comparison of the electrical resistivity values of the hcp phase for the iron and Fe-C alloys during compression and decompression shows that these two sets of results do not deviate from each other too much (Figure S1). Specifically, we did not observe noticeable deviations of the resistivity in successive measurements of different time intervals from the modeled curves. Therefore, we conclude that hysteresis for the hcp-Fe and hcp-$Fe_{99}C_1$ phase under decompression does not have a noticeable effect in the reported electrical resistivity values and thus does not affect further data analysis and modeling. Systematic error in electrical resistivity using van der Pauw method was estimated by considering the propagation of uncertainty from sample thickness and error due to displacement of electrodes in relation to sample edge as shown in Figures 2 and 3 (Seagle et al., 2013; van der Pauw, 1958).

To describe the pressure-dependent electrical resistivity of iron, we employed a model from previous studies (Seagle et al., 2013; Stacey & Anderson, 2001). The electrical resistivity ρ_e of metals is modeled as $\rho_e \propto \Theta_D^{-n} V^{-n/3}$, where Θ_D is the Debye temperature and is assumed to be only volume-dependent, V is the volume, and n is a fitting parameter. For hcp-Fe, the model can be written as

$$\rho_e = \rho_e^0 \left(\frac{\Theta_D}{\Theta_D^0}\right)^{-n} \left(\frac{V_{Fe}(P)}{V_{Fe}^0(P)}\right)^{-n/3} \quad (1)$$

where the zero in the superscript indicates a reference state at 1 bar and 300 K. A detailed theoretical deduction of the model and its validity test on the resistivity of gold can be found elsewhere (Seagle et al., 2013). Using equation (1) and the equation of state of hcp-Fe (Dewaele et al., 2006) to model the thickness of sample, as well as our high-pressure electrical resistivity measurements, we found the following for hcp-Fe: n = 3.2 ± 0.1 and ρ_e^0 = 24.7±1.0 μΩ cm (R^2 = 0.969). Compared to previous studies, our values for the electrical resistivity of iron are most consistent with Seagle et al. (2013). The results by Gomi et al. (2013) are much higher than what we observed at pressures below ~40 GPa. Nevertheless, the pressure-dependent resistivity of hcp-Fe is flattened at higher pressures such that, at pressures above ~60 GPa, the modeled curves for these studies are almost indistinguishable from each other within experimental uncertainties. We also found the following electrical resistivity of hcp-$Fe_{99}C_1$ up to ~80 GPa

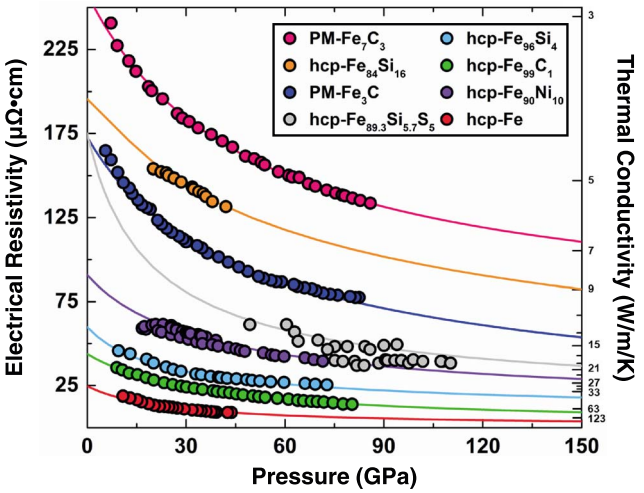

Figure 5. Pressure-dependent electrical resistivity of Fe-light element alloys at high pressure. Experimental data of hcp-Fe (red solid circles), hcp-$Fe_{99}C_1$ (green solid circles), paramagnetic (PM)-Fe_3C (dark blue solid circles), and PM-Fe_7C_3 (magenta solid circles) in this study are plotted for comparison to better understand the light element alloying effects on the electrical resistivity at high pressures. Light blue solid circles: hcp-$Fe_{96}Si_4$ alloy (Gomi et al., 2013); purple solid circles: hcp-$Fe_{90}Ni_{10}$ alloy (Gomi & Hirose, 2015); gray solid circles: hcp-$Fe_{89.3}Si_{5.7}S_5$; orange solid circles: hcp-$Fe_{84}Si_{16}$ alloy (Seagle et al., 2013). The solid lines represent model fits to respective experimental data. The right vertical axis shows the thermal conductivity of the alloys converted from their respective electrical conductivity using Wiedemann-Franz law at 300 K.

(Figure 2a): n = 2.4 ± 0.029 and ρ_e^0 = 43.8±1.0 μΩ cm (R^2 = 0.999). The ρ_e^0 of hcp-$Fe_{99}C_1$ is bigger than that of hcp-Fe, revealing the light element effect of carbon.

The electrical resistivity of Fe_7C_3 and Fe_3C at high pressures up to ~80 GPa was also evaluated using the thickness of the quenched samples and the equation of state of Fe_7C_3 (Nakajima et al., 2011) and Fe_3C (Li et al., 2002; Figure 3). The high-pressure electrical resistivity of Fe_7C_3 has not been previously determined experimentally, so no comparison of the same material was made. Our derived electrical resistivity of Fe_3C at 1 bar is in good agreement with a previous experimentally determined value by Lee and Simkovich (1987) within experimental uncertainties. However, we should also note that calculated results of 47–140 μΩ cm exist for Fe_3C at ambient conditions (Häglund et al., 1991; Helsing & Grimvall, 1991; Radcliffe & Rollason, 1958), which are much lower than our result and the previous experimental value. Such a discrepancy may be due to the lack of understanding in accounting for the contribution of the electron interactions in the Fe-C system. Analysis of our high-pressure results shows that the pressure gradient of the resistivity for both Fe_7C_3 and Fe_3C changes drastically at approximately 6 GPa (Figure 4), which is attributed to the FM to PM transition reported in previous studies for Fe_3C (Duman et al., 2005; Gao et al., 2008; Litasov et al., 2013; Prescher et al., 2012) and for Fe_7C_3 (Chen et al., 2012, 2014). The electrical resistivity and its pressure derivative do not show a noticeable change above this pressure, including in the range of ~22–25 GPa, where a high-spin to a low-spin transition of Fe_3C is reported experimentally in previous reports (Lin et al., 2004; Prescher et al., 2012).

4. Discussion and Implications

4.1. Alloying Effects of C and Si on the Resistivity of Fe at High Pressure

To understand the alloying effects of candidate light elements and Ni on the electrical resistivity and thermal conductivity of iron at high pressures, we compared the electrical resistivity of hcp-$Fe_{96}Si_4$ (Gomi et al., 2013), hcp-$Fe_{84}Si_{16}$ (Seagle et al., 2013), hcp-$Fe_{89.3}Si_{5.7}S_5$ (Suehiro et al., 2017), and hcp-$Fe_{90}Ni_{10}$ (Gomi & Hirose, 2015) with the results from hcp-Fe, hcp-$Fe_{99}C_1$, PM-Fe_3C, and PM-Fe_7C_3 in this study (Figure 5). The FM-Fe_7C_3 has the highest electrical resistivity from 1 bar to 150 GPa among all the Fe alloys that have been investigated. At Earth's core pressures, the electrical resistivity of Fe_7C_3 is nearly 27 times that of pure iron, showing an ultra-strong alloying effect of carbon on the electrical resistivity of iron. Since the thermal conductivity of iron alloys is inversely proportional to the electrical resistivity, the addition of a few atomic percent carbon is expected to significantly reduce the thermal conductivity. Comparison of the results shows that the resistivity of iron alloys considered in this study decreases with increasing pressure and eventually becomes flat at pressures approximately above 100 GPa, indicating that the applied pressure would have a decreasing effect on the resistivity.

The total resistivity of iron alloys can be described in two parts: The first is the resistivity of pure iron as a function of pressure and temperature (equation (1)), and the second is the characteristic term of the element i, which is the residual resistivity and is only dependent on volume (Seagle et al., 2013). Matthiessen's rule (Matthiessen & Vogt, 1864) gives a reasonably good description of the residual resistivity of alloy elements, which takes the following form:

$$\rho_{\mathrm{Fe}-i}(V,T) = \rho_{\mathrm{Fe}}(V,T) + \sum_i \rho_i(V) \times \chi_i \quad (2)$$

where i denotes the alloying elements, $\rho_i(V)$ is the compositionally dependent unit resistivity, and χ_i is the concentration of the alloying elements in atomic percent. Recent experimental studies have shown that Matthiessen's rule is applicable for evaluating the electrical resistivity of Fe-Si alloy and the Fe-Ni alloy

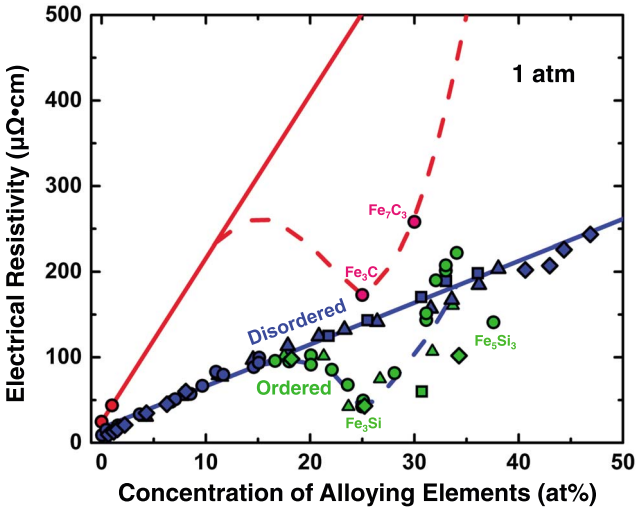

Figure 6. The electrical resistivity of the iron-silicon and iron-carbon alloys as a function of the atomic percent of the alloying element at ambient pressure. The blue and green circles (Varga et al., 2002), diamonds, triangles, and squares indicate the electrical resistivity of the disordered (blue color) and ordered iron-silicon (green color) alloy, respectively (Secco, 2017). The blue solid line represents a linear fit of resistivity data for disordered iron-silicon alloys according to Matthiessen's rule (Matthiessen & Vogt, 1864). The blue dashed line guides the eye for ordered iron-silicon alloy data. The valley of the iron-silicon alloy at 25 at % indicates Fe_3Si ordering (Varga et al., 2002). Red circles: electrical resistivity of Fe and $Fe_{99}C_1$ from this study; pink circles: electrical resistivity of Fe_3C and Fe_7C_3. Linear extrapolations of the electrical conductivity with Fe and $Fe_{99}C_1$ (red solid line) show that the electrical conductivity of Fe_3C and Fe_7C_3 is well below the value predicted by Matthiessen's rule. The red dashed line is a visual guide for the ordered iron carbon compounds, which schematically show a valley at approximately Fe_3C with 25 at % C.

system at high pressure (Gomi et al., 2013, 2016; Gomi & Hirose, 2015; Seagle et al., 2013). For $F_{99}C_1$, we fitted the residual resistivity to the following equation used in a previous study (Seagle et al., 2013):

$$\rho_C(V) = \rho_C^0 \left(\frac{e^{\left[V_{Fe-C}(P)/V^0_{Fe-C}(P)\right]} - 1}{e - 1} \right)^2 \quad (3)$$

where e is the natural exponential function, the subscripted C stands for carbon, and $V_{Fe-C}(P)/V^0_{Fe-C}(P)$ is the unit cell volume ratio of the Fe-C alloy. This equation allows us to evaluate the resistivity of the Fe-C alloy with different carbon concentrations. For $Fe_{99}C_1$, where χ_C = 1 at % , the best fit produced ρ_C^0 = 19.1±2.0 (μΩ cm/at %).

We did not apply this method for Fe_3C and Fe_7C_3 since the electrical resistivity should not behave in the same manner with increasing impurity concentration when the stoichiometric compositions of Fe_3C and Fe_7C_3 are formed due to chemical ordering (Figure 6). The electrical resistivity as a function of the impurity concentration in the Fe-Si system shows an anomalous local minimum in Fe_3Si (Secco, 2017; Figure 6). Similar behavior has also been observed in the Cu-Au system for Cu_3Au and CuAu (Johansson & Linde, 1936), leading to a lower atomic residual resistivity for these compositions. Since the electrical resistivity of Fe-C alloys at a higher carbon concentration has not been measured yet, the electrical resistivity of Fe-C alloys can increase in two manners: (1) It behaves like Fe-Si system in which a local minimum appears in Fe_3C (Figure 6) or (2) the electrical resistivity has a linear relationship with the carbon concentration. However, fitting our four Fe-C alloy data points to a linear function shows significant misfits. We thus adopt the local minimum model in this study.

Gomi et al. (2016) reviewed the saturation theory associated with the impurity effect of Si and Ni at high-pressure following their previous works (Gomi et al., 2013; Gomi & Hirose, 2015) and the high-temperature effect (Ohta et al., 2016). They concluded that Matthiessen's rule would become invalid at high impurity concentration or high temperature due to the saturation effect. According to their calculation, the chemically induced saturation effect will only lower the impurity resistivity of Si by 5% at 5,000 K and 169 GPa, yielding a comparatively small influence on the resistivity of iron alloy. However, the linearity of the electrical resistivity of the iron-silicon alloy with respect to the atomic concentration of silicon (up to ~45 at%) in Figure 6 contradicts the saturation theory for the impurity effect of silicon (Gomi et al., 2016) and therefore proves the validity of Matthiessen's rule up to higher concentrations.

In Figure 7, the residual electrical resistivity of carbon, silicon, sulfur, and nickel in iron alloys at high pressures has been compared to illustrate the alloying effects of these elements on the resistivity of iron. The residual electrical resistivity of each element is calculated by subtracting the resistivity of iron from the resistivity of the iron alloy. The difference is divided by the atomic or weight percentage of the element in the alloy to make the comparison more quantitative by the per weight percent (Figure 7a) and per atomic percent (Figure 7b). As a transition metal, nickel expectedly has the lower residual resistivity across the entire pressure range considered. That nickel has a slight residual resistivity as an alloying element in iron agrees well with the conclusions that nickel plays a minor role in constraining other properties of iron alloy (Lin et al., 2003; Mao et al., 1990). In Figure 7a, the electrical resistivity per weight percent of carbon overrides that of silicon, sulfur, and nickel for the entire pressure range considered, which indicates that an Fe-C binary composition would have higher electrical resistivity than other Fe-light element compositions. In Figure 7b, carbon is shown to have the highest residual resistivity per atomic percent at low pressure. At approximately 85 GPa, the residual resistivity of carbon drops below that of silicon and remains an intermediate between hcp-$Fe_{96}Si_4$ (Gomi et al., 2013) and hcp-$Fe_{84}Si_{16}$ (Seagle et al., 2013) at higher pressures. The residual resistivity of silicon estimated from the two different studies is reasonably close and within experimental

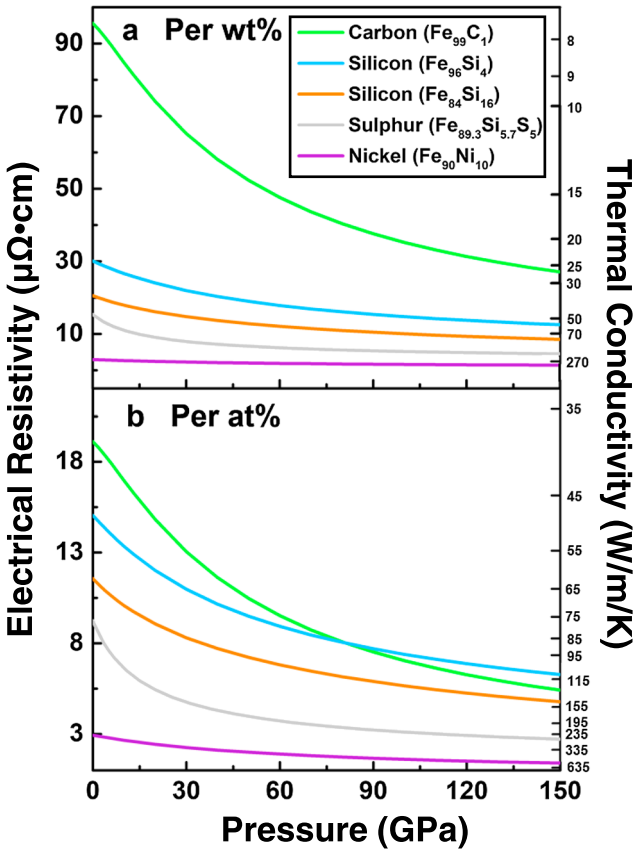

Figure 7. Residual resistivity of carbon, silicon, sulfur, and nickel in their Fe alloys as a function of pressure at room temperature. Figure 7a shows the resistivity per weight percent of each light element, while Figure 7b is for per atomic percent. The residual resistivity of carbon (green) was calculated from the difference between $Fe_{99}C_1$ and Fe. The residual resistivity of silicon was estimated from $Fe_{96}Si_4$ (Gomi et al., 2013; orange) and $Fe_{84}Si_{16}$ (Seagle et al., 2013; blue). The residual resistivity of sulfur (gray) was estimated from $Fe_{89.3}Si_{5.7}S_5$ (Suehiro et al., 2017), while the residual resistivity of nickel (purple) was estimated from $Fe_{90}Ni_{10}$ (Gomi & Hirose, 2015). The corresponding thermal conductivity of these alloys is shown in the right vertical axis using Wiedemann-Franz law for the conversion from the electrical conductivity to the thermal conductivity.

uncertainty. Comparison of the resistivity of the Fe-C and Fe-Si systems at high pressures shows that carbon exhibits a higher residual resistivity per weight percent and an equally strong residual resistivity per atomic percent. Given the strength of the alloying effect of different light elements and the theoretical concentration of the two light elements, a core composition of iron-carbon alloy will distinguish itself by a much lower thermal conductivity than an Fe-Si composition.

4.2. Electrical Resistivity and Thermal Conductivity of Fe and its Alloys in Earth's Outer Core

The Bloch-Grüneisen formula describes a linear relationship between temperature and electrical resistivity and takes the following form:

$$\rho_{BG}(V,T) = D(V)\left(\frac{T}{\Theta_D(V)}\right)^n \int_0^{\frac{\Theta_D(V)}{T}} \frac{z^n}{(\exp(z)-1)(1-\exp(z))}dz \quad (4)$$

in which ρ_{BG} is the ideal resistivity of a metal, $D(V)$ is a volume-dependent material constant, and n is usually considered an integer determined by the correlation of electrons at high temperature ($T > 0.4\Theta_D$). A recent laser-heated DAC study found that the electrical resistivity of iron deviates negatively from the linear increase at temperatures from 1,000 K to 4,500 K (Ohta et al., 2016), while the electrical resistivity is well described by the empirical shunt resistor model (Wiesmann et al., 1977) as follows:

$$\frac{1}{\rho_e} = \frac{1}{\rho_{BG}} + \frac{1}{\rho_{sat}}. \quad (5)$$

where ρ_{sat} is the Ioffe-Regel value (ρ_{sat} = 168 μΩ cm proposed by Bohnenkamp et al., 2002). The negative deviation from the Bloch-Grüneisen formula implies that the electrical resistivity will finally approach the Ioffe-Regel value instead of increasing infinitely because the mean-free path of free electrons becomes close to the interatomic distance as temperature increases. This high-temperature suppression of electrical resistivity is called the aforementioned saturation effect (Gunnarsson et al., 2003; Ohta et al., 2016).

Here we consider the thermal effect on the resistivity at high pressures using the shunt resistor model to take the saturation effect into account (Ohta et al., 2016). The solid to liquid transition of iron was proposed to have a negligible effect on the thermal or electrical conductivity of iron (Nishi et al., 2003; Secco & Schloessin, 1989; Stacey & Anderson, 2001). However, we note that there are experimental measurements at 1 bar, which show that the electrical resistivity of iron increases on melting by ~7–8% (Güntherodt et al., 1975; Van Zytveld, 1980). The increase above in electrical resistivity on melting could suggest a decrease in thermal conductivity by 7–8% at ambient pressure if the Lorenz number remains constant. However, we did not attempt to take the melting effect into account in our calculation because of the uncertain pressure-temperature effects and Lorenz number at the relevant core conditions.

After our resistivity modeling, we applied the Wiedemann-Franz law to calculate the thermal conductivity along a recent adiabatic temperature profile of the Earth's outer core (Figure 8) (Anzellini et al., 2013). In this modeling, the thermal conductivity of the iron and iron alloys was determined by the electrical conductivity at high pressure via the Wiedemann-Franz law: $k_e = L\sigma T$, where k_e is the thermal conductivity contributed by electrons (which, for a metal, is generally a good estimate of the total thermal conductivity k), σ is the electrical conductivity (which is inversely proportional to the electrical resistivity ρ_e), and L is the

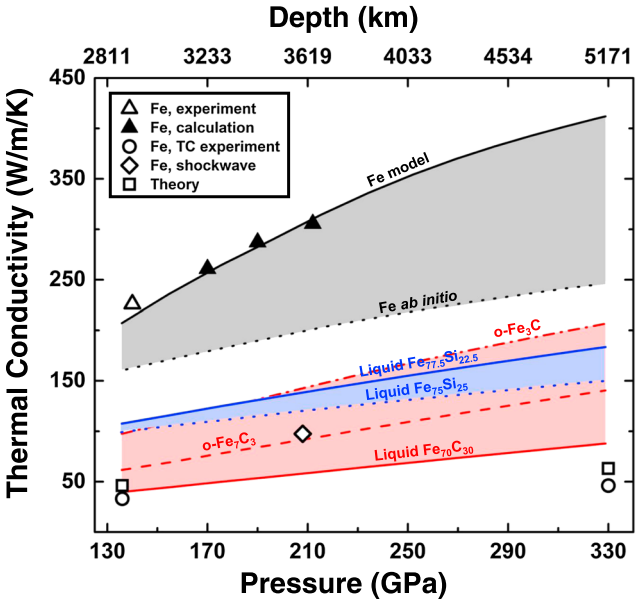

Figure 8. Thermal conductivity of Fe and Fe alloys along an expected geotherm of the Earth's outer core. A representative geotherm proposed by Anzellini et al. (2013) is used for the modeling of the thermal conductivity of the Fe, Fe-C, and Fe-Si alloys. The red solid, dashed, and dash-dot lines are the thermal conductivity model for $Fe_{70}C_{30}$, orthorhombic Fe_7C_3, and orthorhombic Fe_3C, respectively; blue solid line: $Fe_{77.5}Si_{22.5}$ model (Gomi et al., 2013); blue dotted line: ab initio results of $Fe_{75}Si_{25}$ (de Koker et al., 2012); black dotted line: ab initio results of Fe (Pozzo et al., 2012); black open triangle: high pressure-temperature electrical resistivity result of Fe at 140 GPa and 3,750 K (Ohta et al., 2016); black solid triangle: modeled results with parameters from high pressure-temperature electrical resistivity measurements (Ohta et al., 2016); open circles: direct thermal conductivity measurement of Fe at core-mantle boundary (CMB) and inner-core boundary (ICB; Konôpková et al., 2016); open diamond: shock wave data of pure Fe at 208 GPa and 5,330 K (Bi et al., 2002); open square: theoretical estimation of thermal conductivity at the CMB and ICB (Stacey & Anderson, 2001). The solid black line is to guide the eye through a modeled thermal conductivity profile of iron in the core, based on experimental results shown in the open and solid triangles. Fe-C alloy in the core is expected to exhibit relatively low thermal conductivity.

Lorenz number (which has an ideal value of $L_0 = 2.44 \times 10^{-8}$ WΩK^{-2}). The Lorenz number was found to depend on the temperature and composition for iron and iron-silicon liquids in the range of $2.2 - 2.4 \times 10^{-8}$ WΩK^{-2} by theoretical calculations (de Koker et al., 2012; Pozzo et al., 2013). In a recent study, the Seebeck coefficient of iron was investigated experimentally at $T < 2{,}100$ K and $P < 6$ GPa and was observed to contribute less than 1% to L_0. However, the lattice component of the thermal conductivity was found to be nonnegligible for the iron-silicon alloy and iron at high temperature or in a liquid state, which is embodied by the L varying as a function of temperature and silicon content (Secco, 2017).

There is a lack of a systematic study on the Lorenz number at high pressure and temperature for the iron alloys, especially for iron-carbon alloys. Therefore, we used the Lorenz number with the ideal value ($L_0 = 2.44 \times 10^{-8}$ WΩK^{-2}) here to be consistent with previous studies (Gomi et al., 2013, 2016; Gomi & Hirose, 2015; Ohta et al., 2016; Seagle et al., 2013). That said, the Lorenz number of iron-silicon alloys can be relatively high at ~3.0–4.0 L_0. At high temperatures and different silicon concentrations, it can be as low as ~1.5–1.7 L_0 (Secco, 2017). This indicates that the thermal conductivity of iron-carbon alloys in this study and the previous literature values calculated with $L = L_0$ could be underestimated. The electrical resistivity of hcp-Fe at relevant CMB conditions (136 GPa and 4,050 K) is 48 μΩ cm, corresponding to a thermal conductivity of 207 Wm^{-1} K^{-1}. This value is close to that reported by Ohta et al. (2016) (226 Wm^{-1} K^{-1} at 140 GPa and 3,750 K) but higher than the first principle estimations of 144 Wm^{-1} K^{-1} (Pozzo et al., 2012) and ~130–140 Wm^{-1} K^{-1} (de Koker et al., 2012). On the other hand, a laser pump-and-probe spectroscopic study reported the thermal conductivity of iron to be 33 Wm^{-1} K^{-1} at the topmost outer core conditions (Konôpková et al., 2016), which is much lower than laser-heated DAC resistivity measurements and first-principles calculations (Ohta et al., 2016; Pozzo et al., 2012) but close to the previous theoretical estimation of 46 Wm^{-1} K^{-1} (Stacey & Anderson, 2001; Figure 8).

To understand and compare the effects of C and Si on the thermal conductivity of iron in the outer core, we modeled the thermal conductivity of iron-carbon alloys in this study and previously reported experimental data for iron-silicon alloys at relevant outer core conditions. $Fe_{77.5}Si_{22.5}$ (12.7 wt % Si) and $Fe_{70}C_{30}$ (8.4 wt % C) were suggested to account for the 10% density deficit in the outer core, making these alloys candidate outer core compositions (Sata et al., 2010). The resistivity of $Fe_{70}C_{30}$ and $Fe_{77.5}Si_{22.5}$ was calculated using equations (2) and (3) with $\chi_C = 0.30$ and 0.225, respectively. Our modeled resistivity of $Fe_{77.5}Si_{22.5}$ is 92 μΩ cm at the CMB (136 GPa, 4,050 K), yielding a thermal conductivity of 108 Wm^{-1} K^{-1} (Figure 9). This value is very close to previous estimates for the thermal conductivity of Fe-Si alloy at CMB conditions (Gomi et al., 2013; Gomi & Hirose, 2015; Seagle et al., 2013). We calculated the resistivity of $Fe_{70}C_{30}$ to be much higher than that of $Fe_{77.5}Si_{22.5}$—with a value of 249 μΩ cm and hence a thermal conductivity of 40 Wm^{-1} K^{-1}. This result is smaller than most of the results estimated from pure iron and iron-silicon alloys but agrees well with the theoretical estimations supporting a low thermal conductivity of the core (Stacey & Anderson, 2001).

4.3. Implications for CMB Heat Flux and Geodynamo

The thermal dynamics and evolution of the Earth's core are closely related to our understanding of the thermal conductivity of candidate iron alloys in the region. To understand the consequences of light element alloying with iron on the conductive heat flux at CMB and geodynamics in the outer core, we also evaluated the conductive heat along an adiabatic temperature gradient for the Fe-Si and Fe-C systems.

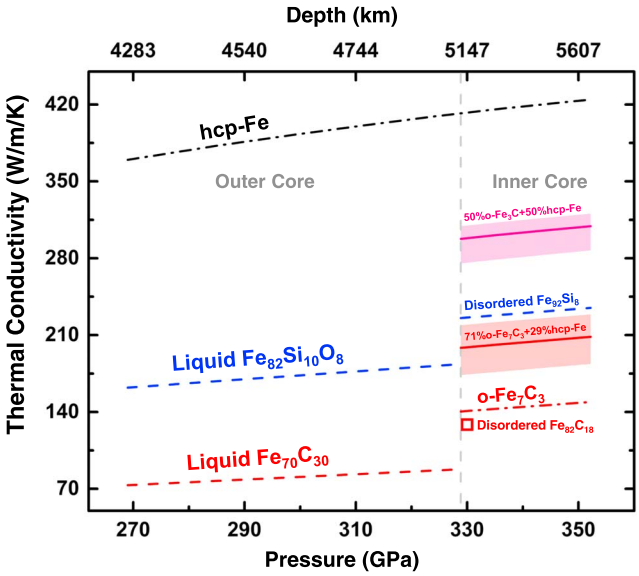

Figure 9. Modeled thermal conductivity of iron and Fe alloys at pressure-temperature conditions of the outer and inner core. The gray dashed vertical line indicates inner-core boundary (ICB). The solid red line: hcp-Fe mixture with 71% orthorhombic Fe_7C_3 (o-Fe_7C_3) in volume; solid magenta line: hcp-Fe mixture with 50% orthorhombic Fe_3C (o-Fe_3C) in volume; red dash-dot line: pure orthorhombic Fe_7C_3 (with 8.4 wt % carbon in Fe); red dashed line: liquid $Fe_{70}C_{30}$; blue dashed line: theoretical calculation results of $Fe_{82}Si_{10}O_8$ for the outer core (Pozzo et al., 2013) and $Fe_{92}Si_8$ for the inner core (Pozzo et al., 2014); black dash-dot line: hcp-Fe; red square: disordered $Fe_{82}C_{18}$ alloy at ICB conditions. The red and magenta shadow area represents the uncertainty of the thermal conductivity of Fe and Fe_7C_3 mixture and Fe and Fe_3C mixture.

The adiabatic conductive heat flow (Q_a) can be calculated using the following equation (Davies et al., 2015):

$$Q_a = -4\pi r^2 k \left(\frac{\partial T}{\partial r}\right)_{r=r_0} \quad (6)$$

where k is the thermal conductivity, T is temperature, and r is the radius of Earth's core. Using the following thermal dynamic relation,

$$\left(\frac{\partial T}{\partial r}\right)_s = -g\gamma T/\phi, \quad (7)$$

where $\gamma = 1.51$ is a constant Grüneisen parameter (Hernlund & Labrosse, 2007), g is gravity acceleration, and ϕ is a seismic parameter, the adiabatic heat flow can be written as

$$Q_a = -4\pi r^2 k \frac{g\gamma T}{\phi}. \quad (8)$$

We obtained r, g, and ϕ at the CMB from the PREM model (Dziewonski & Anderson, 1981), T from a previous adiabatic profile (Anzellini et al., 2013), and k from the modeled results in this study. We estimated the conductive heat flow at CMB to be 6 TW for $Fe_{70}C_{30}$ and 16 TW for $Fe_{77.5}Si_{22.5}$. The total heat flow at the CMB is estimated to be 8–16 TW from previous studies (Lay et al., 2008; Nimmo, 2007; Wu et al., 2011). Therefore, the conductive heat flow estimated from the thermal conductivity of iron-carbon alloy is lower than the total heat flow budget in geodynamics modeling.

Values of the thermal conductivity of core constituents have a radical impact on the evolution and dynamics of the core. The inner core age was calculated to be less than 1 billion years according to the high thermal conductivities reported (Gomi et al., 2013, 2016; Labrosse, 2015), despite the early existence of the geomagnetic field revealed by magnetism recorded in terrestrial minerals up to 3.4–4.2 billion years in age (Tarduno et al., 2014, 2015). A stratified layer at the top of the core, which is detectable by decadal variation of day length and geomagnetic secular variation, has been shown to correlate with higher thermal conductivity; a CMB heat flow as low as 13 TW can engender the layer (Buffett, 2014; Lister & Buffett, 1998). However, under the circumstance where conductive heat flow is lower than CMB heat flow, the stratified layer can also be stabilized by a compositional flux from the mantle (Lister & Buffett, 1998). The high heat flow across the CMB by the thermal conduction casts doubt on the energy balance of the outer core and the possibility of the thermal convection powering the geodynamo alone, before inner core nucleation (Buffett, 2003; Olson, 2013). Additional energy sources such as a radiogenic heat source (Buffett, 2003) and the precipitation of magnesium-bearing minerals (O'Rourke & Stevenson, 2016) may account for this energy deficit. The low iron-carbon thermal conductivity and resulting low conductive heat flow (~6 TW) obtained from iron-carbon alloy provide new insight into this controversy, as the value is less than the total CMB heat flow estimation (8–16 TW), yet more plausible than the value of ~16 TW obtained for the iron-silicon alloy. A low thermal conductivity enhances an older inner-core age and early origin of the geomagnetic field. The lower conductive heat flow at the CMB also marginalizes the additional energy sources, such as radioactive heat and other mechanisms whose capability remains uncertain.

4.4. Electrical Resistivity and Thermal Conductivity of the Inner Core

Earth's inner core distinguishes itself from the outer core by a solid composition and lower concentration of light elements. The transition from the outer to the inner core brings discontinuity of physical properties (e.g., density and sound velocity) at the inner-outer core boundary. The electrical resistivity and thermal conductivity at the top of the inner core are crucial properties regarding constraining the thermal convection and geomagnetic stability of the inner core (Dharmaraj & Stanley, 2012).

Thermal convection in the solid inner core is proposed to be the driving force of crystal alignment and therefore results in inner core anisotropy (Jeanloz & Wenk, 1988). It is superior to the driving force from the outer core for its higher stress level and lateral variation capability. The change in the inner core convection pattern could also help explain the variation in the seismically observed anisotropy with depth (Buffett, 2009). Thermal conductivity determines the heat conducted down the temperature gradient in the solid core, and the total heat flow at the ICB is required to surmount the conduction heat to permit thermal convection (Pozzo et al., 2014). A previous study on the thermal conductivity of the inner core that considered iron-silicon compositions $Fe_{83}Si_7$ and $Fe_{82}Si_8$ in the solid state reported an increase of thermal conductivity by ~45–56% compared to previous estimations at the bottom of the outer core (Pozzo et al., 2013). The corresponding higher conduction heat through the ICB suggests that thermal convection is less likely in the inner core (Pozzo et al., 2014).

With different electrical resistivity behavior at high pressures between the iron-carbon alloy ($Fe_{99}C_1$) and the stoichiometric and chemically ordered iron-carbon compound (Fe_3C and Fe_7C_3), we consider that a solid system composed of iron and carbon should take into account the difference between the ordered and disordered states when addressing transport properties (Figure 6). The transformation from a disordered liquid solution to an ordered compound is expected to contribute to the discontinuity of transport properties at the ICB. As aforementioned, the difference of electrical resistivity has been shown for the iron-silicon system (Figure 6; Varga et al., 2002). Iron-silicon alloys processed with two different cooling methods (furnace cooling and quenching) can adopt either ordered (Fe_3Si and Fe_5Si_3) or disordered (Fe-Si alloy) atomic distributions, which exhibit different electrical resistivity (Varga et al., 2002). The ordered alloy has a much lower electrical resistivity compared with the disordered alloy, whose electrical resistivity increases linearly with the atomic concentration of silicon (Figure 6).

We modeled the thermal conductivity of the inner core and show the discontinuity of thermal conductivity contributed by the chemical ordering of iron carbides (Figure 9). Previous work shows that the mixture of 54.5% to 86.4% (by volume fraction) Fe_7C_3 and hcp-Fe for the ICB temperature from 5,000 K to 7,000 K conforms to the density of the inner core (Nakajima et al., 2011). Similar results were derived for 71–84% at 6,000 K as well (Chen et al., 2012). For Fe_3C, a volume fraction of approximately 50% mixed with hcp-Fe is most commonly proposed to satisfy the inner core density (Gao et al., 2008, 2011; Litasov et al., 2013). The electrical conductivity of a binary metallic mixture is expressed as follows (Landauer, 1952):

$$\sigma_m = \frac{1}{4}\left\{(3x_1-1)\sigma_1 + (3x_2-1)\sigma_2 + \left[((3x_1-1)\sigma_1 + (3x_2-1)\sigma_2)^2 + 8\sigma_1\sigma_2\right]^{\frac{1}{2}}\right\} \quad (9)$$

where σ_m is the electrical conductivity of the mixture, σ_1 and σ_2 are the electrical conductivity of two metals, respectively, and x_1 and x_2 are their volume fraction. A detailed explanation and discussion of various metallic systems of this equation can be found in Landauer (1952). We modeled the thermal conductivity of the mixture of Fe_7C_3 and hcp-Fe with a 71% volume fraction of Fe_7C_3, which is a lower bound of a previous estimation (Chen et al., 2014). The derivation using equation (9) assumes that all the regions within the mixture are spherical, and for the mixture containing a needle or disk-shaped region, it gives an approximate estimation (Landauer, 1952). Since iron alloys typically have dendritic structures, we calculated the uncertainty of applying equation (9) to the mixture of Fe and Fe-C compounds (Figure 9; Landauer, 1952). Here the model with a maximum iron percent can be used to manifest the huge difference in thermal conductivity between the disordered iron-carbon alloy ($Fe_{82}C_{18}$) and the mixture of Fe_7C_3 and Fe as a modeled composition of the inner core along the same pressure and temperature profile employed for outer core thermal conductivity (Anzellini et al., 2013; Dziewonski & Anderson, 1981; Figure 9). The thermal conductivity at the ICB of a mixture of 50% Fe_3C and hcp-Fe and $Fe_{82}C_{18}$, which can account for the 4.5–4.9% density deficit in the region, is shown as well.

The thermal conductivity of the Fe_7C_3 and hcp-Fe mixture ranges from 170 Wm^{-1} K^{-1} (84%) to 198 Wm^{-1} K^{-1} (71%) at 329 GPa and 5,526 K corresponding to σ=1.3–1.5 × 10^6 Ω^{-1} m^{-1}. The magnetic diffusivity is calculated to be η= 0.54–0.64 m^2 s^{-1}. The magnetic diffusion time in the inner core that determines the periods needed for diffusion in the solid iron alloy to alter the magnetic field is $t_\eta = r_{IC}^2/\eta$ (Pozzo et al., 2014), and for an inner core radius of r_{IC}^2 =1,221 km, the magnetic diffusion time assumes 74–87 kyr. The thermal conductivity and magnetic diffusion time calculated from the mixture of Fe_7C_3 and hcp-Fe are close to

previous estimations (Pozzo et al., 2014) that support a high conduction heat at the ICB and therefore suppress the possibility of the inner core convection and a longer magnetic diffusion times compared to that of the outer core, but whether this could stabilize the magnetic field remains debatable (Alfè et al., 2007; Dharmaraj & Stanley, 2012; Pozzo et al., 2014). The Fe_3C and hcp-Fe model gives a rather high thermal conductivity of 298 Wm^{-1} K^{-1} and corresponding electrical conductivity of 2.2×10^6 Ω^{-1} m^{-1}. In contrast, $Fe_{82}C_{18}$ gives a low thermal conductivity of 128 Wm^{-1} K^{-1} and an electrical conductivity of 1.0×10^6 Ω^{-1} m^{-1}. Recent studies support Fe_7C_3 instead of Fe_3C as the inner-core carbon-bearing phase for its strong stability at relevant conditions—experiments have observed that Fe_3C melts incongruently into the iron-rich Fe_7C_3 alloy and a liquid at high pressure and temperature (Chen et al., 2012; Liu et al., 2016b; Lord et al., 2009; Mookherjee, 2011; Nakajima et al., 2011). The high Poisson's ratio and shear softening exhibited at high pressure strengthen the argument for the presence of Fe_7C_3 in the inner core (Chen et al., 2014; Prescher et al., 2015). Additionally, the solubility of carbon in solid iron decreases with increasing pressure to less than 2.7 at% at 44 GPa (Lord et al., 2009), in which case the composition of $Fe_{82}C_{18}$ under inner core pressures is less plausible. Above all, the Fe_7C_3 and hcp-Fe mixture is a competent candidate inner core composition that displays a relatively high thermal conductivity, which provides evidence against the thermal convection of the inner core and supports a high electrical conductivity that results in a long-term magnetic diffusion (Pozzo et al., 2014). The thermal and electrical conductivity gap at the ICB depends on the parameters considered. For a liquid outer core composed of liquid iron-carbon alloy and a solid inner core composed of iron and Fe_7C_3 mixture, the gap would be almost ~2.6 times larger than that of a core composed of iron-silicon alloy (Figure 9). Based on the argument that the inner core condition is favorable for large-size grain growth and the time span for grain growth is long enough (Yamazaki et al., 2017), ordered iron silicide or iron carbide should be formed, for example, Fe_3Si and Fe_5Si_3, or Fe_3C and Fe_7C_3, rather than disordered solid alloys, resulting in a greater gap of thermal and electrical transport properties at the ICB, which may influence the dynamo motion and geomagnetic morphology (Pozzo et al., 2014).

Acknowledgments
We acknowledge Youjun Zhang for his constructive suggestions. We appreciate technical assistance from Yanping Yang in the FIB analysis of the quenched samples. We thank Rusty Roberts and Freyja O'Toole for their edits and comments on this paper. We also thank anonymous reviewers for their comments and suggestions and editor M. Walter for his constructive comments. J.F.L. acknowledges support from the Geophysics and CSEDI Programs of the National Science Foundation (NSF), Deep Carbon Observatory of the Sloan Foundation, and Center for High Pressure Science and Advanced Technology (HPSTAR). The data for this paper are available in supplements.

References

Alfè, D., Gillan, M., & Price, G. (2007). Temperature and composition of the Earth's core. *ConPh*, *48*(2), 63–80.
Anzellini, S., Dewaele, A., Mezouar, M., Loubeyre, P., & Morard, G. (2013). Melting of iron at Earth's inner core boundary based on fast X-ray diffraction. *Science*, *340*(6131), 464–466. https://doi.org/10.1126/science.1233514
Badro, J., Fiquet, G., Guyot, F., Gregoryanz, E., Occelli, F., Antonangeli, D., & d'Astuto, M. (2007). Effect of light elements on the sound velocities in solid iron: Implications for the composition of Earth's core. *Earth and Planetary Science Letters*, *254*(1-2), 233–238. https://doi.org/10.1016/j.epsl.2006.11.025
Bi, Y., Tan, H., & Jing, F. (2002). Electrical conductivity of iron under shock compression up to 200 GPa. *Journal of Physics: Condensed Matter*, *14*(44), 10849.
Bohnenkamp, U., Sandström, R., & Grimvall, G. (2002). Electrical resistivity of steels and face-centered-cubic iron. *Journal of Applied Physics*, *92*(8), 4402–4407. https://doi.org/10.1063/1.1502182
Buffett, B. (2014). Geomagnetic fluctuations reveal stable stratification at the top of the Earth's core. *Nature*, *507*(7493), 484–487. https://doi.org/10.1038/nature13122
Buffett, B. (2016). Earth science: Another energy source for the geodynamo. *Nature*, *529*(7586), 288–289. https://doi.org/10.1038/529288a
Buffett, B. A. (2003). The thermal state of Earth's core. *Science*, *299*(5613), 1675–1677. https://doi.org/10.1126/science.1081518
Buffett, B. A. (2009). Onset and orientation of convection in the inner core. *GeoJI*, *179*(2), 711–719.
Chen, B., Gao, L., Lavina, B., Dera, P., Alp, E. E., Zhao, J., & Li, J. (2012). Magneto-elastic coupling in compressed Fe_7C_3 supports carbon in Earth's inner core. *Geophysical Research Letters*, *39*, L18301. https://doi.org/10.1029/2012GL052875
Chen, B., Li, Z., Zhang, D., Liu, J., Hu, M. Y., Zhao, J., et al. (2014). Hidden carbon in Earth's inner core revealed by shear softening in dense Fe7C3. *Proceedings of the National Academy of Sciences*, *111*(50), 17,755–17,758. https://doi.org/10.1073/pnas.1411154111
Davies, C., Pozzo, M., Gubbins, D., & Alfè, D. (2015). Constraints from material properties on the dynamics and evolution of Earth's core. *Nature Geoscience*, *8*(9), 678–685. https://doi.org/10.1038/ngeo2492
de Koker, N., Steinle-Neumann, G., & Vlček, V. (2012). Electrical resistivity and thermal conductivity of liquid Fe alloys at high P and T, and heat flux in Earth's core. *Proceedings of the National Academy of Sciences of the United States of America*, *109*(11), 4070–4073. https://doi.org/10.1073/pnas.1111841109
Dewaele, A., Loubeyre, P., Occelli, F., Mezouar, M., Dorogokupets, P. I., & Torrent, M. (2006). Quasihydrostatic equation of state of iron above 2 Mbar. *Physical Review Letters*, *97*(21), 215504. https://doi.org/10.1103/PhysRevLett.97.215504
Dharmaraj, G., & Stanley, S. (2012). Effect of inner core conductivity on planetary dynamo models. *Physics of the Earth and Planetary Interiors*, *212*, 1–9.
Dobson, D. (2016). Geophysics: Earth's core problem. *Nature*, *534*(7605), 45–45. https://doi.org/10.1038/534045a
Duman, E., Acet, M., Wassermann, E., Itié, J., Baudelet, F., Mathon, O., & Pascarelli, S. (2005). Magnetic instabilities in Fe 3 C cementite particles observed with Fe K-edge X-ray circular dichroism under pressure. *Physical Review Letters*, *94*(7), 075502. https://doi.org/10.1103/PhysRevLett.94.075502
Dziewonski, A. M., & Anderson, D. L. (1981). Preliminary reference Earth model. *Physics of the Earth and Planetary Interiors*, *25*(4), 297–356. https://doi.org/10.1016/0031-9201(81)90046-7
Fei, Y., & Brosh, E. (2014). Experimental study and thermodynamic calculations of phase relations in the Fe-C system at high pressure. *Earth and Planetary Science Letters*, *408*, 155–162.

Gao, L., Chen, B., Wang, J., Alp, E. E., Zhao, J., Lerche, M., et al. (2008). Pressure-induced magnetic transition and sound velocities of Fe_3C: Implications for carbon in the Earth's inner core. *Geophysical Research Letters*, *35*, L17306. https://doi.org/10.1029/2008GL034817

Gao, L., Chen, B., Zhao, J., Alp, E. E., Sturhahn, W., & Li, J. (2011). Effect of temperature on sound velocities of compressed Fe_3C, a candidate component of the Earth's inner core. *Earth and Planetary Science Letters*, *309*(3-4), 213–220. https://doi.org/10.1016/j.epsl.2011.06.037

Giles, P., Longenbach, M., & Marder, A. (1971). High-pressure $\alpha \rightleftarrows \varepsilon$ martensitic transformation in iron. *Journal of Applied Physics*, *42*(11), 4290–4295. https://doi.org/10.1063/1.1659768

Gomi, H., & Hirose, K. (2015). Electrical resistivity and thermal conductivity of hcp Fe-Ni alloys under high pressure: Implications for thermal convection in the Earth's core. *Physics of the Earth and Planetary Interiors*, *247*, 2–10. https://doi.org/10.1016/j.pepi.2015.04.003

Gomi, H., Hirose, K., Akai, H., & Fei, Y. (2016). Electrical resistivity of substitutionally disordered hcp Fe-Si and Fe-Ni alloys: Chemically-induced resistivity saturation in the Earth's core. *Earth and Planetary Science Letters*, *451*, 51–61.

Gomi, H., Ohta, K., Hirose, K., Labrosse, S., Caracas, R., Verstraete, M. J., & Hernlund, J. W. (2013). The high conductivity of iron and thermal evolution of the Earth's core. *Physics of the Earth and Planetary Interiors*, *224*, 88–103. https://doi.org/10.1016/j.pepi.2013.07.010

Gunnarsson, O., Calandra, M., & Han, J. (2003). Colloquium: Saturation of electrical resistivity. *Reviews of Modern Physics*, *75*(4), 1085–1099. https://doi.org/10.1103/RevModPhys.75.1085

Güntherodt, H.-J., Hauser, E., Künzi, H., & Müller, R. (1975). The electrical resistivity of liquid Fe, Co, Ni and Pd. *Physics Letters A*, *54*(4), 291–292. https://doi.org/10.1016/0375-9601(75)90263-7

Häglund, J., Grimvall, G., & Jarlborg, T. (1991). Electronic structure, X-ray photoemission spectra, and transport properties of Fe_3C (cementite). *Physical Review B*, *44*(7), 2914.

Helsing, J., & Grimvall, G. (1991). Thermal conductivity of cast iron: Models and analysis of experiments. *Journal of Applied Physics*, *70*(3), 1198–1206. https://doi.org/10.1063/1.349573

Hernlund, J., & Labrosse, S. (2007). Geophysically consistent values of the perovskite to post-perovskite transition Clapeyron slope. *Geophysical Research Letters*, *34*, L05309. https://doi.org/10.1029/2006GL028961

Hirose, K., Labrosse, S., & Hernlund, J. (2013). Composition and state of the core. *Annual Review of Earth and Planetary Sciences*, *41*(1), 657–691. https://doi.org/10.1146/annurev-earth-050212-124007

Jeanloz, R., & Wenk, H. R. (1988). Convection and anisotropy of the inner core. *Geophysical Research Letters*, *15*(1), 72–75. https://doi.org/10.1029/GL015i001p00072

Johansson, C., & Linde, J. (1936). Röntgenographische und elektrische Untersuchungen des CuAu-Systems. *AnP*, *417*(1), 1–48.

Konôpková, Z., McWilliams, R. S., Gómez-Pérez, N., & Goncharov, A. F. (2016). Direct measurement of thermal conductivity in solid iron at planetary core conditions. *Nature*, *534*(7605), 99–101. https://doi.org/10.1038/nature18009

Labrosse, S. (2015). Thermal evolution of the core with a high thermal conductivity. *Physics of the Earth and Planetary Interiors*, *247*, 36–55. https://doi.org/10.1016/j.pepi.2015.02.002

Landauer, R. (1952). The electrical resistance of binary metallic mixtures. *Journal of Applied Physics*, *23*(7), 779–784. https://doi.org/10.1063/1.1702301

Lay, T., Hernlund, J., & Buffett, B. A. (2008). Core-mantle boundary heat flow. *Nature Geoscience*, *1*(1), 25–32. https://doi.org/10.1038/ngeo.2007.44

Lee, M.-C., & Simkovich, G. (1987). Electrical conduction behavior of cementite, Fe3C. *Metallurgical Transactions A*, *18*(4), 485–486. https://doi.org/10.1007/BF02648811

Li, J., & Fei, Y. (2003). Experimental constraints on core composition. *Treatise on Geochemistry*, *2*, 568.

Li, J., Mao, H., Fei, Y., Gregoryanz, E., Eremets, M., & Zha, C. (2002). Compression of Fe3C to 30 GPa at room temperature. *PCM*, *29*(3), 166–169.

Lin, J.-F., Struzhkin, V. V., Mao, H.-k., Hemley, R. J., Chow, P., Hu, M. Y., & Li, J. (2004). Magnetic transition in compressed Fe3C from X-ray emission spectroscopy. *Physical Review B*, *70*(21), 212405.

Lin, J. F., Struzhkin, V. V., Sturhahn, W., Huang, E., Zhao, J., Hu, M. Y., et al. (2003). Sound velocities of iron-nickel and iron-silicon alloys at high pressures. *Geophysical Research Letters*, *30*(21), 2112. https://doi.org/10.1029/2003GL018405

Lister, J. R., & Buffett, B. A. (1998). Stratification of the outer core at the core-mantle boundary. *Physics of the Earth and Planetary Interiors*, *105*(1–2), 5–19. https://doi.org/10.1016/S0031-9201(97)00082-4

Litasov, K. D., Sharygin, I. S., Dorogokupets, P. I., Shatskiy, A., Gavryushkin, P. N., Sokolova, T. S., et al. (2013). Thermal equation of state and thermodynamic properties of iron carbide Fe3C to 31 GPa and 1473 K. *Journal of Geophysical Research: Solid Earth*, *118*, 5274–5284. https://doi.org/10.1002/2013JB010270

Liu, J., Li, J., & Ikuta, D. (2016a). Elastic softening in Fe7C3 with implications for Earth's deep carbon reservoirs. *Journal of Geophysical Research: Solid Earth*, *121*, 1514–1524. https://doi.org/10.1002/2015JB012701

Liu, J., Lin, J. F., Prakapenka, V. B., Prescher, C., & Yoshino, T. (2016b). Phase relations of Fe3C and Fe7C3 up to 185 GPa and 5200 K: Implication for the stability of iron carbide in the Earth's core. *Geophysical Research Letters*, *43*, 12,415–12,422. https://doi.org/10.1002/2016GL071353

Lord, O., Walter, M., Dasgupta, R., Walker, D., & Clark, S. (2009). Melting in the Fe-C system to 70 GPa. *Earth and Planetary Science Letters*, *284*(1–2), 157–167. https://doi.org/10.1016/j.epsl.2009.04.017

Mao, H., Wu, Y., Chen, L., Shu, J., & Jephcoat, A. P. (1990). Static compression of iron to 300 GPa and Fe0. 8Ni0. 2 alloy to 260 GPa: Implications for composition of the core. *Journal of Geophysical Research*, *95*(B13), 21,737–21,742. https://doi.org/10.1029/JB095iB13p21737

Mao, H., Xu, J.-A., & Bell, P. (1986). Calibration of the ruby pressure gauge to 800 kbar under quasi-hydrostatic conditions. *Journal of Geophysical Research*, *91*(B5), 4673–4676. https://doi.org/10.1029/JB091iB05p04673

Mao, Z., Lin, J.-F., Liu, J., Alatas, A., Gao, L., Zhao, J., & Mao, H.-K. (2012). Sound velocities of Fe and Fe-Si alloy in the Earth's core. *Proceedings of the National Academy of Sciences*, *109*(26), 10,239–10,244. https://doi.org/10.1073/pnas.1207086109

Matthiessen, A., & Vogt, C. (1864). On the influence of temperature on the electric conducting-power of alloys. *Philosophical Transactions. Royal Society of London*, *154*(0), 167–200. https://doi.org/10.1098/rstl.1864.0004

Medvedeva, N., Van Aken, D., & Medvedeva, J. E. (2010). Magnetism in bcc and fcc Fe with carbon and manganese. *Journal of Physics: Condensed Matter*, *22*(31), 316002.

Mookherjee, M. (2011). Elasticity and anisotropy of Fe3C at high pressures. *American Mineralogist*, *96*(10), 1530–1536. https://doi.org/10.2138/am.2011.3917

Nakajima, Y., Takahashi, E., Sata, N., Nishihara, Y., Hirose, K., Funakoshi, K., & Ohishi, Y. (2011). Thermoelastic property and high-pressure stability of Fe7C3: Implication for iron-carbide in the Earth's core. *American Mineralogist*, *96*(7), 1158–1165. https://doi.org/10.2138/am.2011.3703

Nimmo, F. (2007). Energetics of the core. *Treatise on Geophysics*, *8*, 31–65. https://doi.org/10.1016/B978-044452748-6/00128-0

Nishi, T., Shibata, H., Waseda, Y., & Ohta, H. (2003). Thermal conductivities of molten iron, cobalt, and nickel by laser flash method. *MMTA*, *34*(12), 2801–2807. https://doi.org/10.1007/s11661-003-0181-2

Ohta, K., Kuwayama, Y., Hirose, K., Shimizu, K., & Ohishi, Y. (2016). Experimental determination of the electrical resistivity of iron at Earth's core conditions. *Nature*, *534*(7605), 95–98. https://doi.org/10.1038/nature17957

Olson, P. (2013). The new core paradox. *Science*, *342*(6157), 431–432. https://doi.org/10.1126/science.1243477

O'Rourke, J. G., & Stevenson, D. J. (2016). Powering Earth's dynamo with magnesium precipitation from the core. *Nature*, *529*(7586), 387–389. https://doi.org/10.1038/nature16495

Poirier, J.-P. (1994). Light elements in the Earth's outer core: A critical review. *Physics of the Earth and Planetary Interiors*, *85*(3-4), 319–337. https://doi.org/10.1016/0031-9201(94)90120-1

Pozzo, M., Davies, C., Gubbins, D., & Alfè, D. (2012). Thermal and electrical conductivity of iron at Earth's core conditions. *Nature*, *485*(7398), 355–358. https://doi.org/10.1038/nature11031

Pozzo, M., Davies, C., Gubbins, D., & Alfè, D. (2013). Transport properties for liquid silicon-oxygen-iron mixtures at Earth's core conditions. *Physical Review B*, *87*(1), 014110.

Pozzo, M., Davies, C., Gubbins, D., & Alfè, D. (2014). Thermal and electrical conductivity of solid iron and iron-silicon mixtures at Earth's core conditions. *Earth and Planetary Science Letters*, *393*, 159–164.

Prescher, C., Dubrovinsky, L., Bykova, E., Kupenko, I., Glazyrin, K., Kantor, A., et al. (2015). High Poisson's ratio of Earth's inner core explained by carbon alloying. *Nature Geoscience*, *8*(3), 220–223. https://doi.org/10.1038/ngeo2370

Prescher, C., Dubrovinsky, L., Mccammon, C., Glazyrin, K., Nakajima, Y., Kantor, A., et al. (2012). Structurally hidden magnetic transitions in Fe3C at high pressures. *Physical Review B*, *85*(14), 6–9.

Radcliffe, S., & Rollason, E. (1958). Electrical resistivity of high purity Fe-C alloys. *Journal of the Iron and Steel Institute*, *189*, 45.

Sata, N., Hirose, K., Shen, G., Nakajima, Y., Ohishi, Y., & Hirao, N. (2010). Compression of FeSi, Fe3C, Fe0. 95O, and FeS under the core pressures and implication for light element in the Earth's core. *Journal of Geophysical Research*, *115*, B09204. https://doi.org/10.1029/2009JB006975

Seagle, C. T., Cottrell, E., Fei, Y., Hummer, D. R., & Prakapenka, V. B. (2013). Electrical and thermal transport properties of iron and iron-silicon alloy at high pressure. *Geophysical Research Letters*, *40*, 5377–5381. https://doi.org/10.1002/2013GL057930

Secco, R., & Schloessin, H. (1989). The electrical resistivity of solid and liquid Fe at pressures up to 7 GPa. *Journal of Geophysical Research*, *94*(B5), 5887–5894. https://doi.org/10.1029/JB094iB05p05887

Secco, R. A. (2017). Thermal conductivity and Seebeck coefficient of Fe and Fe-Si alloys: Implications for variable Lorenz number. *Physics of the Earth and Planetary Interiors*, *265*, 23–34. https://doi.org/10.1016/j.pepi.2017.01.005

Stacey, F. D., & Anderson, O. L. (2001). Electrical and thermal conductivities of Fe-Ni-Si alloy under core conditions. *Physics of the Earth and Planetary Interiors*, *124*(3-4), 153–162. https://doi.org/10.1016/S0031-9201(01)00186-8

Stevenson, D. J. (2008). A planetary perspective on the deep Earth. *Nature*, *451*(7176), 261–265. https://doi.org/10.1038/nature06582

Suehiro, S., Ohta, K., Hirose, K., Morard, G., & Ohishi, Y. (2017). The influence of sulfur on the electrical resistivity of hcp iron: Implications for the core conductivity of Mars and Earth. *Geophysical Research Letters*, *44*, 8254–8259. https://doi.org/10.1002/2017GL074021

Tarduno, J. A., Blackman, E. G., & Mamajek, E. E. (2014). Detecting the oldest geodynamo and attendant shielding from the solar wind: Implications for habitability. *Physics of the Earth and Planetary Interiors*, *233*, 68–87. https://doi.org/10.1016/j.pepi.2014.05.007

Tarduno, J. A., Cottrell, R. D., Davis, W. J., Nimmo, F., & Bono, R. K. (2015). A Hadean to Paleoarchean geodynamo recorded by single zircon crystals. *Science*, *349*(6247), 521–524. https://doi.org/10.1126/science.aaa9114

Tsuzuki, A., Sago, S., Hirano, S.-I., & Naka, S. (1984). High temperature and pressure preparation and properties of iron carbides Fe 7 C 3 and Fe 3 C. *JMatS*, *19*(8), 2513–2518.

van der Pauw, L. (1958). A method of measuring specific resistivity and Hall effect of discs of arbitrary shape. *Philips Research Reports*, *13*, 1–9.

Van Zytveld, J. (1980). Electrical resistivities of liquid transition metals. *Le Journal de Physique Colloques*, *41*(C8), C8–503–C508–506.

Varga, L., Mazaleyrat, F., Kovac, J., & Greneche, J. (2002). Structural and magnetic properties of metastable Fe1-xSix ($0.15 < x < 0.34$) alloys prepared by a rapid-quenching technique. *Journal of Physics: Condensed Matter*, *14*(8), 1985.

Vočadlo, L., Brodholt, J., Dobson, D. P., Knight, K., Marshall, W., Price, G. D., & Wood, I. G. (2002). The effect of ferromagnetism on the equation of state of Fe 3 C studied by first-principles calculations. *Earth and Planetary Science Letters*, *203*(1), 567–575. https://doi.org/10.1016/S0012-821X(02)00839-7

Wiesmann, H., Gurvitch, M., Lutz, H., Ghosh, A., Schwarz, B., Strongin, M., et al. (1977). Simple model for characterizing the electrical resistivity in A-15 superconductors. *Physical Review Letters*, *38*(14), 782–785. https://doi.org/10.1103/PhysRevLett.38.782

Wood, B. J. (1993). Carbon in the core. *Earth and Planetary Science Letters*, *117*(3-4), 593–607. https://doi.org/10.1016/0012-821X(93)90105-I

Wood, B. J., Li, J., & Shahar, A. (2013). Carbon in the core: Its influence on the properties of core and mantle. *Reviews in Mineralogy and Geochemistry*, *75*(1), 231–250. https://doi.org/10.2138/rmg.2013.75.8

Wood, I., Vočadlo, L., Knight, K., Dobson, D. P., Marshall, W., Price, G. D., & Brodholt, J. (2004). Thermal expansion and crystal structure of cementite, Fe3C, between 4 and 600 K determined by time-of-flight neutron powder diffraction. *Journal of Applied Crystallography*, *37*(1), 82–90. https://doi.org/10.1107/S0021889803024695

Wu, B., Driscoll, P., & Olson, P. (2011). A statistical boundary layer model for the mantle D'region. *Journal of Geophysical Research*, *116*, B12112. https://doi.org/10.1029/2011JB008511

Yamazaki, D., Tsujino, N., Yoneda, A., Ito, E., Yoshino, T., Tange, Y., & Higo, Y. (2017). Grain growth of ε-iron: Implications to grain size and its evolution in the Earth's inner core. *Earth and Planetary Science Letters*, *459*, 238–243.